

Tetragonal NaVPO₄F@rGO nanocomposite as a high-rate cathode for aqueous zinc-ion batteries

Jiajie Zhou,^a Shenghong Yang,^a Peiyin Xu,^a Xiaoyan Shi,^a Junling Xu,^a Lianyi Shao,^{,a,b} Yan Sun^{*,b} and Zhipeng Sun^{*,a}*

School of Materials and Energy, Guangdong University of Technology, Guangzhou 510006, Guangdong, China.

E-mail: shaoliany@gdut.edu.cn, zpsunxj@gdut.edu.cn

Key Laboratory of Advanced Electrode Materials for Novel Solar Cells for Petroleum and Chemical Industry of China, School of Chemistry and Life Sciences, Suzhou University of Science and Technology, Suzhou 215009, Jiangsu, China.

E-mail: juzi147@163.com

Experimental section

Synthesis of NVPF and NVPF@rGO

NVPF and NVPF@rGO were synthesized via a hydrothermal method, followed by sintering at high temperatures. Firstly, 0.7 mmol of vanadium acetylacetonate ($C_{10}H_{14}O_5V$, Aladdin) was dissolved in 24 mL ethanol and magnetically stirred for 20 mins, yielding solution A. Simultaneously, 0.7 mmol each of sodium fluoride (NaF, Aladdin) and ammonium dihydrogen phosphate ($NH_4H_2PO_4$, Aladdin) were dissolved in 12 mL water and stirred for 20 mins to produce solution B. The solution A and solution B were mixed and stirred for 10 mins to form solution C. Afterwards, a graphene oxide (GO, 2 mg mL^{-1}) solution underwent sonication for 1 hour, was combined with solution C, and stirred for an additional 10 mins to produce solution D. This solution was then placed into an autoclave, gradually heated to $120 \text{ }^\circ\text{C}$ for 2 hours. Subsequently, the precursor was washed three times with water and ethanol, respectively, and dried at $60 \text{ }^\circ\text{C}$ for 12 hours. For calcination, the precursor was heated in a nitrogen-filled tube furnace at different temperatures for 8 hours, yielding NVPF@rGO powder. Adjusting the calcination temperatures to 250 , 350 , 450 , and $550 \text{ }^\circ\text{C}$, distinct NVPF@rGO samples were obtained and labeled as NVPF@rGO-1, NVPF@rGO-2, NVPF@rGO-3, and NVPF@rGO-4, respectively. Pure NVPF was synthesized using a similar process, excluding the GO solution.

Materials characterization

X-ray diffraction (XRD) analysis, confirming the purity of the samples, was carried out with a Rigaku Smart Lab diffractometer employing Cu K α radiation. The sample morphologies were examined using scanning electron microscopy (SEM) on a Hitachi SU8220 instrument and transmission electron microscopy (TEM) on a JEM-2010FEF instrument. X-ray photoelectron spectroscopy (XPS) measurements were conducted using an AXIS SUPRA⁺ spectrometer. Raman spectroscopy data were acquired with a HORIBA FRANCE SAS LabRAM Odyssey instrument.

Electrochemical Measurement

The working electrode was prepared by mixing the active material, superconducting carbon black, and polyvinylidene fluoride (PVDF) with a mass ratio of 7:2:1 in appropriate N-methyl-2-pyrrolidone (NMP), followed by coating on 306 stainless steel mesh and drying at 60 °C for 12 hours. The surface mass density of the active material was about 2 mg cm⁻². The coin cells were assembled utilizing glass fiber as a diaphragm, zinc tablet as an anode, and 3 M zinc trifluoromethane sulfonate (Zn (OTf)₂) with 1 mg mL⁻¹ dodecyl benzenesulfonic acid (SDBS) as an aqueous electrolyte. The galvanostatic charge-discharge (GCD) tests and galvanostatic intermittent titration techniques (GITT) were conducted using Neware battery test equipment (CT-4008T) over a voltage range of

0.6–1.8 V. The Shanghai Chenhua CHI electrochemical workstation (CHI 760E) was used for performing electrochemical impedance spectroscopy (EIS, 0.01–10⁵ Hz) and cyclic voltammetry (CV).

Formula section

$$D = \frac{4}{\pi\tau} \left(\frac{m_B V_M}{M_B A} \right)^2 \left(\frac{\Delta E_S}{\Delta E_\tau} \right)^2 \#(1)$$

In this formula, τ denotes the time required for the current pulse. The m_B (g) and M_B (g mol⁻¹) mean the mass and molecular weight of the substance, V_M signifies the molar volume, A represents the contact area between the electrode and the electrolyte, ΔE_S means the steady-state voltage difference, and ΔE_τ is the voltage difference before and after the pulse, respectively.^[1]

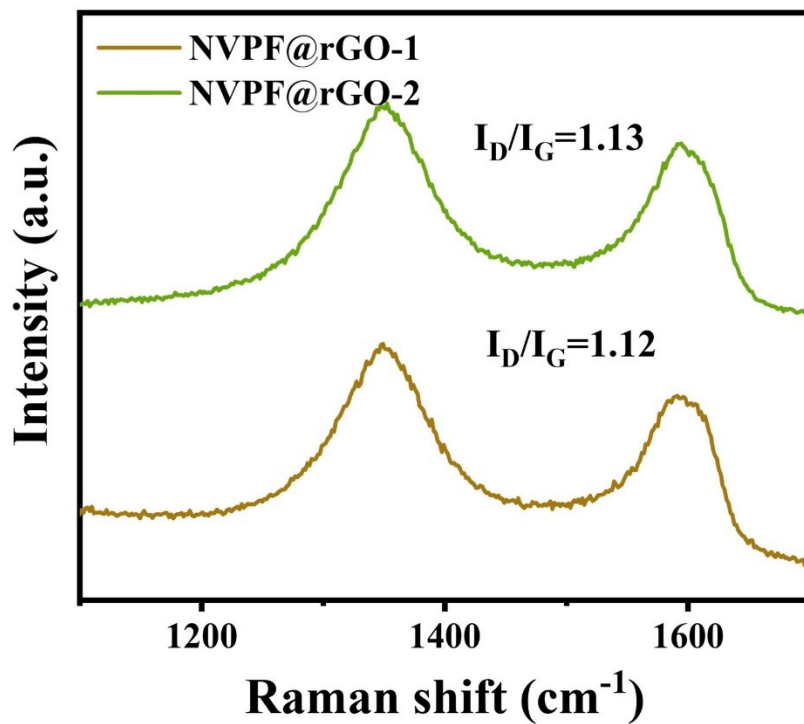


Figure S1. Raman spectra of NVPF@rGO-1 and NVPF@rGO-2.

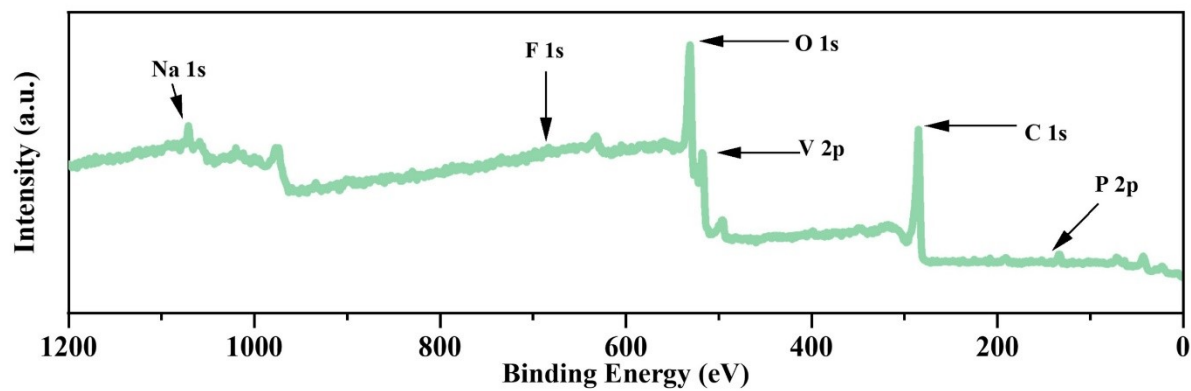


Figure S2. XPS full spectrum of NVPF@rGO-3.

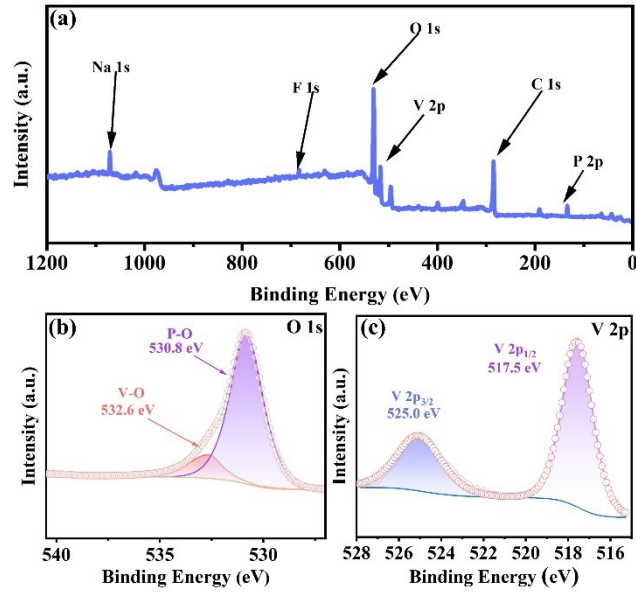


Figure S3. (a) XPS full spectrum of NVPF. XPS spectra of (b) O 1s and (c) V 2p.

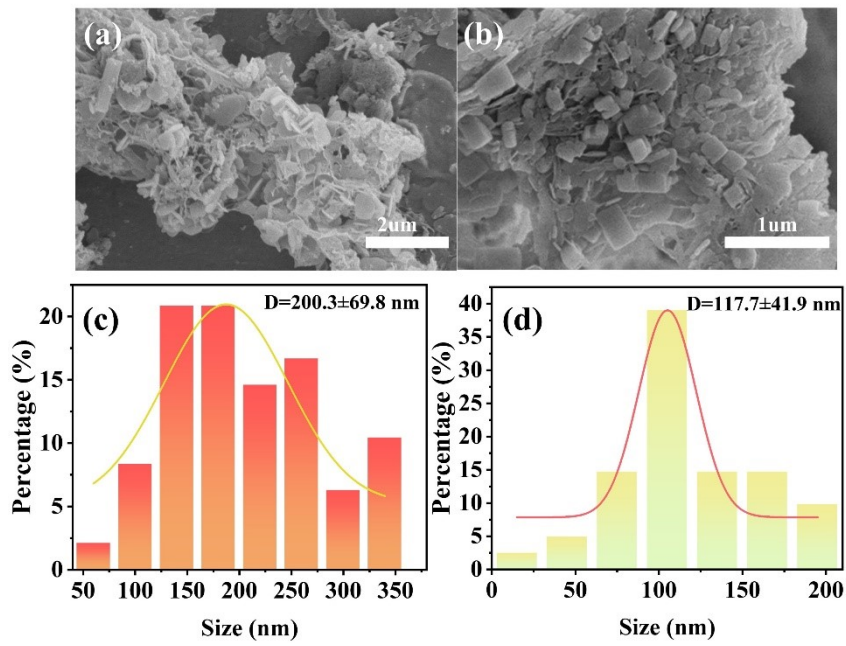


Figure S4. SEM images of (a) NVPF@rGO-1 and (b) NVPF@rGO-2. The particle size distribution of (c) NVPF@rGO-1 and (d) NVPF@rGO-2.

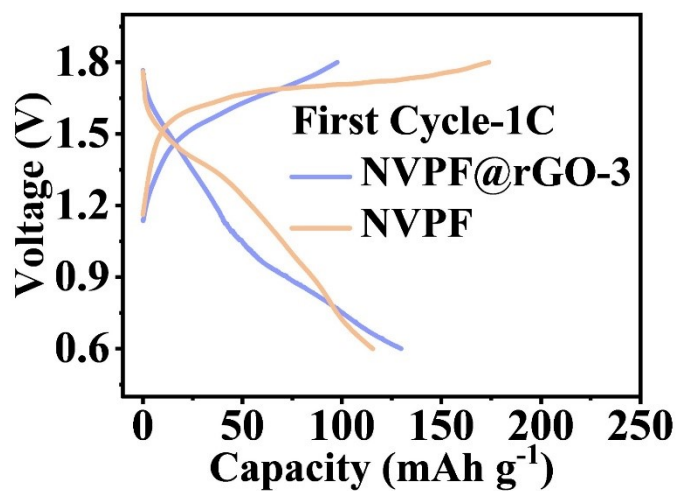


Figure S5. Galvanostatic charge-discharge profiles of NVPF and NVPF@rGO-3 at 1 C.

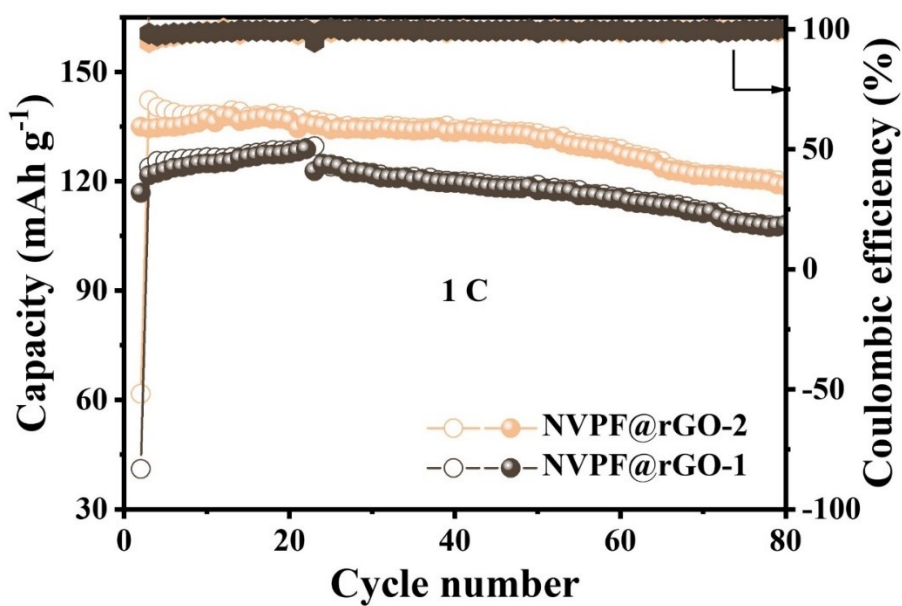


Figure S6. Cycling performance at 1 C of NVPF@rGO-1 and NVPF@rGO-2 electrodes.

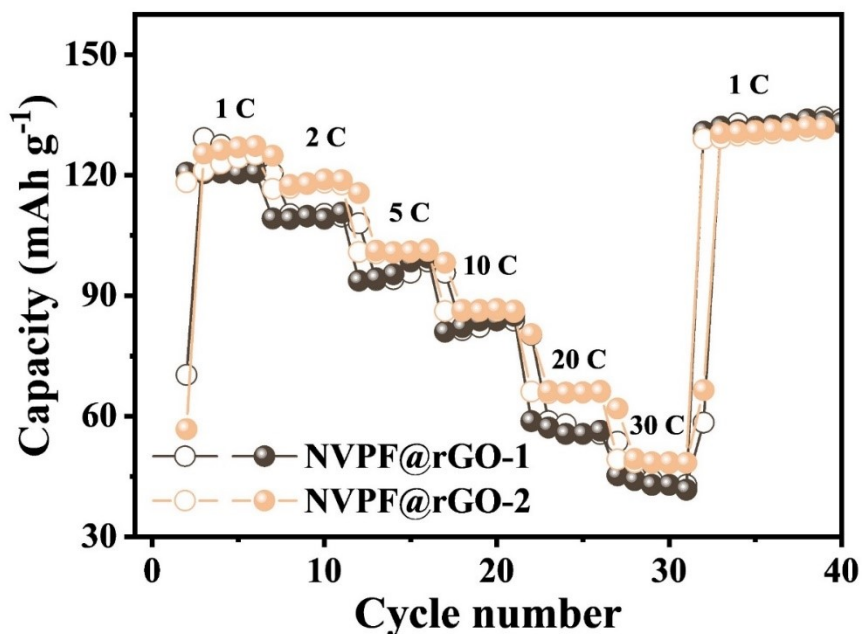


Figure S7. Rate performance for NVPF@rGO-1 and NVPF@rGO-2 electrodes.

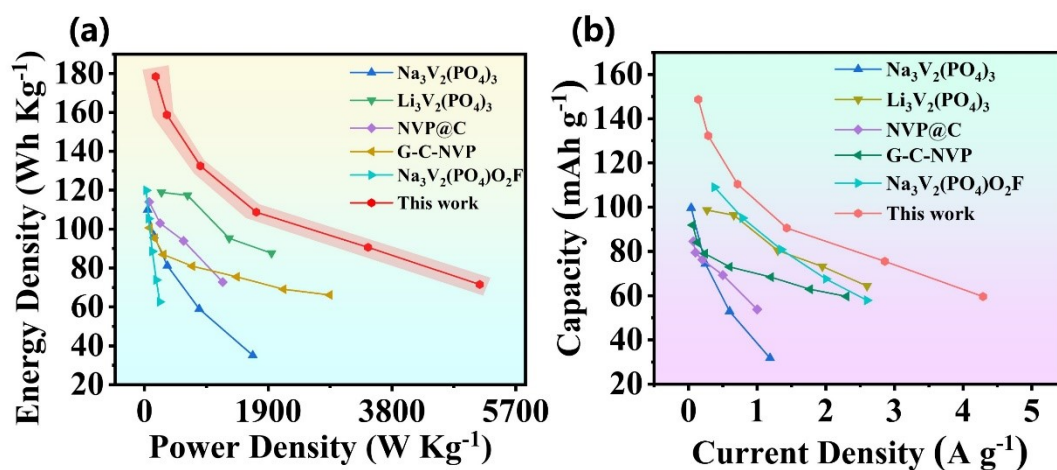


Figure S8. (a) Ragone plot and (b) capacity plot of NVPF@rGO-3 with other reported AZIBs electrodes.^[2-6]

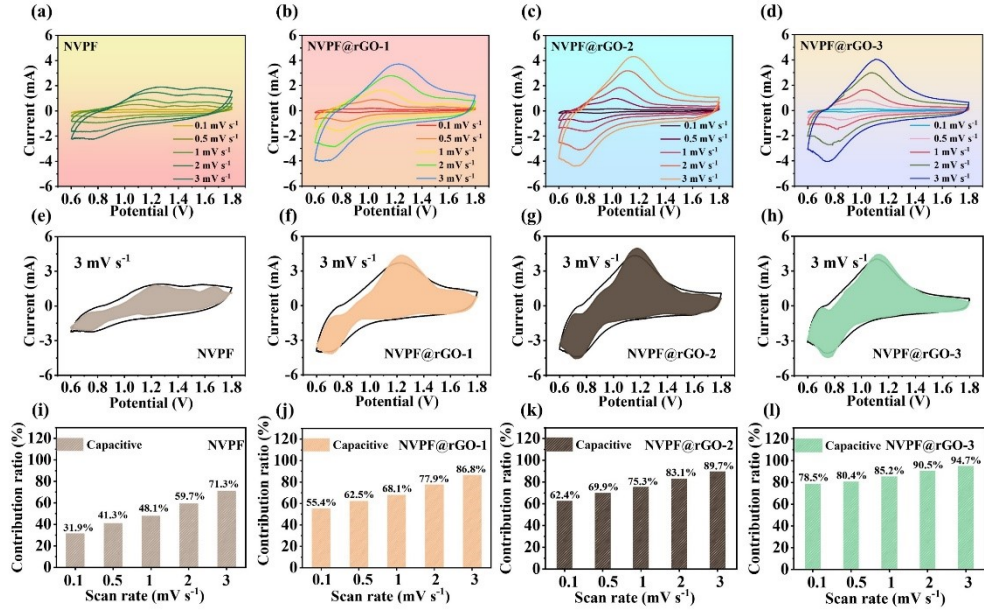


Figure S9. CV curves at different scanning rates for (a) NVPF, (b) NVPF@rGO-1, (c) NVPF@rGO-2, and (d) NVPF@rGO-3 electrodes. The pseudocapacitive controlled portion at 3 mV s⁻¹ for (e) NVPF, (f) NVPF@rGO-1, (g) NVPF@rGO-2, and (h) NVPF@rGO-3 electrodes. The pseudocapacitive controlled portion at different scan rates for (i) NVPF, (j) NVPF@rGO-1, (k) NVPF@rGO-2, and (l) NVPF@rGO-3 electrodes.

Employing the formula $i = k_1v + k_2v^{1/2}$, the current (i) at the specific potential can be separated into two components: the surface-controlled pseudocapacitive effect (k_1v) and the diffusion-controlled effect ($k_2v^{1/2}$).^[7]

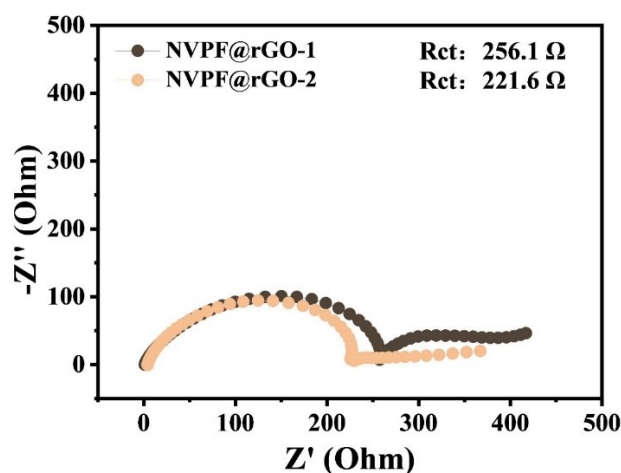


Figure S10. Nyquist plots of NVPF@rGO-1 and NVPF@rGO-2 electrodes.

Table S1. Refined atomic occupancies in NVPF@rGO-3.

Atom	Site	x	y	z	Occupancy
P1	4d	0.00000	0.50000	0.25000	1.000
O1	16n	0.00000	0.32472	0.16184	1.000
F1	4e	0.00000	0.00000	0.37341	0.500
Na1	8j	0.24850	0.50000	0.00000	0.003
F2	2a	0.00000	0.00000	0.00000	0.250
V1	4e	0.00000	0.00000	0.19352	0.812
Na2	8h	0.28340	0.28340	0.00000	0.497

References

- [1] Huang Q, Shao L, Shi X, et al. Na₃V₂O₂(PO₄)₂F nanoparticles@reduced graphene oxide: a high-voltage polyanionic cathode with enhanced reaction kinetics for aqueous zinc-ion batteries [J]. Chemical Engineering Journal, 2023, 468: 143738.
- [2] Li W, Wang K, Cheng S, et al. A long-life aqueous Zn-ion battery based on Na₃V₂(PO₄)₂F₃ cathode [J]. Energy Storage Materials, 2018, 15: 14-21.

- [3] Dong Y, Di S, Zhang F, et al. Nonaqueous electrolyte with dual-cations for high-voltage and long-life zinc batteries [J]. *Journal of Materials Chemistry A*, 2020, 8(6): 3252-3261.
- [4] Ko JS, Paul PP, Wan G, et al. NASICON $\text{Na}_3\text{V}_2(\text{PO}_4)_3$ enables quasi-two-stage Na^+ and Zn^{2+} intercalation for multivalent zinc batteries [J]. *Chemistry of Materials*, 2020, 32(7): 3028-3035.
- [5] Jiang Y, Zou Q, Liu S, et al. The $\text{Li}_3\text{V}_2(\text{PO}_4)_3@C$ materials prepared by freeze-drying assisted sol-gel method for an aqueous zinc ion hybrid battery [J]. *Journal of Electroanalytical Chemistry*, 2021, 900: 115685.
- [6] Li G, Yang Z, Jiang Y, et al. Hybrid aqueous battery based on $\text{Na}_3\text{V}_2(\text{PO}_4)_3/C$ cathode and zinc anode for potential large-scale energy storage [J]. *Journal of Power Sources*, 2016, 308: 52-57.
- [7] Park MJ, Asl HY, Therese S, et al. Structural impact of Zn-insertion into monoclinic $\text{V}_2(\text{PO}_4)_3$: implications for Zn-ion batteries [J]. *Journal of Materials Chemistry A*, 2019, 7(12): 7159-7167.